ACS NANO
Cite This: ACS Nano 2019, 13, 3363−3372
www.acsnano.org

ARTICLE

Ultrafast Diameter-Dependent Water Evaporation from Nanopores

Yinxiao Li,[†,∥] Haowen Chen,[†,∥] Siyang Xiao,[†,∥] Mohammad Amin Alibakhshi,[†] Ching-Wen Lo,[†,‡] Ming-Chang Lu,[‡] and Chuanhua Duan*[,†]

[†]Department of Mechanical Engineering, Boston University, Boston, Massachusetts 02215, United States
[‡]Department of Mechanical Engineering, National Chiao Tung University, Hsinchu 300, Taiwan

Supporting Information

ABSTRACT: Evaporation from nanopores plays an important role in various natural and industrial processes that require efficient heat and mass transfer. The ultimate performance of nanopore-evaporation-based processes is dictated by evaporation kinetics at the liquid−vapor interface, which has yet to be experimentally studied down to the single nanopore level. Here we report unambiguous measurements of kinetically limited intense evaporation from individual hydrophilic nanopores with both hydrophilic and hydrophobic top outer surfaces at 22 °C using nanochannel-connected nanopore devices. Our results show that the evaporation fluxes of nanopores with hydrophilic outer surfaces show a strong diameter dependence with an exponent of nearly −1.5, reaching up to 11-fold of the maximum theoretical predication provided by the classical Hertz−Knudsen relation at a pore diameter of 27 nm. Differently, the evaporation fluxes of nanopores with hydrophobic outer surfaces show a different diameter dependence with an exponent of −0.66, achieving 66% of the maximum theoretical predication at a pore diameter of 28 nm. We discover that the ultrafast diameter-dependent evaporation from nanopores with hydrophilic outer surfaces mainly stems from evaporating water thin films outside of the nanopores. In contrast, the diameter-dependent evaporation from nanopores with hydrophobic outer surfaces is governed by evaporation kinetics inside the nanopores, which indicates that the evaporation coefficient varies in different nanoscale confinements, possibly due to surface-charge-induced concentration changes of hydronium ions. This study enhances our understanding of evaporation at the nanoscale and demonstrates great potential of evaporation from nanopores.

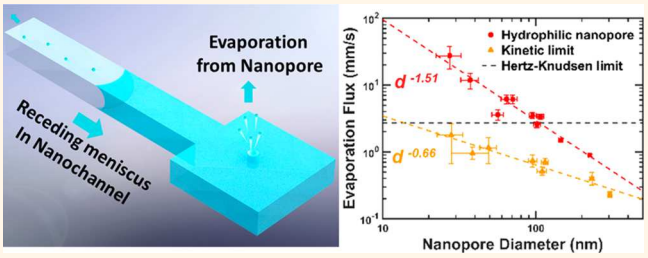

KEYWORDS: *water evaporation, nanopore, evaporating thin film, evaporation kinetics, evaporation flux, evaporation coefficient, kinetic limit*

Evaporation from nanopores is essential for plant transpiration[1,2] and has inspired a variety of technologies in diverse areas including electronics cooling,[3−9] steam generation,[10−12] water desalination,[13−17] and power generation.[18,19] To further develop nanopore-evaporation-based technologies and achieve their ultimate performance, it is critical to understand the ultimate mass-transport-limited process involved. Evaporation from nanopores consists of three mass transport processes, i.e., liquid/vapor transport to/from the liquid−vapor interface, as well as liquid vaporization at the liquid−vapor interface. However, it has been widely recognized that the liquid vaporization at the interface, which is governed by the interfacial evaporation/condensation kinetics, is eventually the mass transport limit.[20] This kinetically limited mass transport process in nanoscale confined spaces has yet to be completely understood. In fact, existing theoretical models are incapable of accurately predicting evaporation from nanopores due to inadequate knowledge of liquid−surface interactions and evaporation kinetics and have predicted different dependence of the evaporation flux on pore diameter.[21,22] On the other hand, current experimental studies based on nanoporous membranes cannot provide much insight from a fundamental perspective because evaporation from these membranes is largely limited by the heat/mass transfer to the liquid−vapor interface[5−9,23] and away from the liquid−vapor interface,[4,24,25] rather than the interfacial evaporation kinetics. These issues could be addressed by single nanopore-based measurements where proper nanofluidic device designs in conjunction with the utilization of strong advection or vacuum are used to ensure heat and mass transfer to/from the interface are no longer the transport limits.[25] However, measurement of ultrasmall mass flow rates (which are only

Received: December 6, 2018
Accepted: March 5, 2019
Published: March 5, 2019

DOI: 10.1021/acsnano.8b09258
ACS Nano 2019, 13, 3363−3372

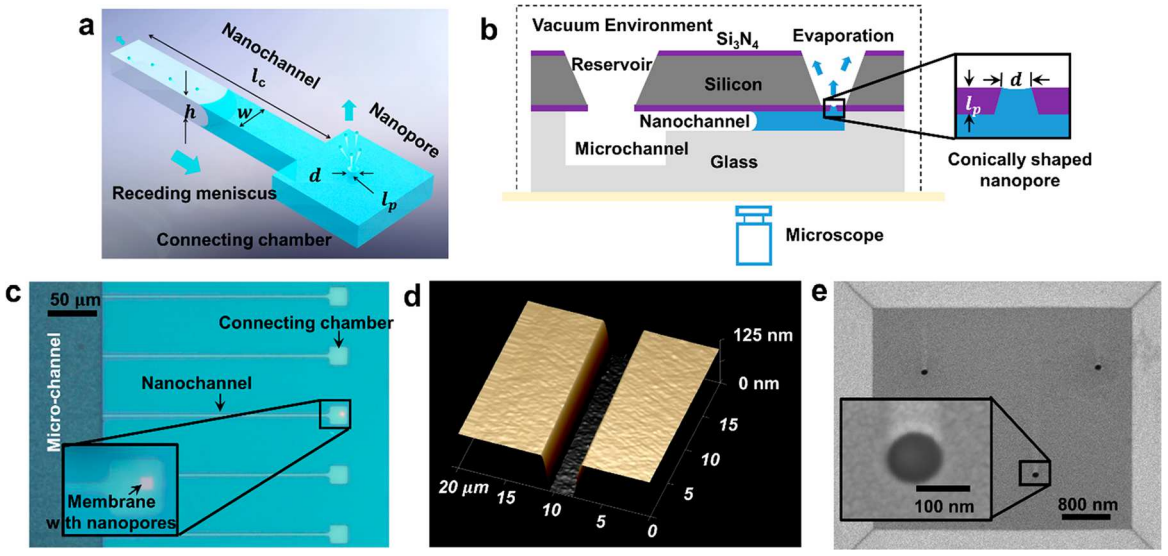

Figure 1. Design, fabrication, and characterization of hybrid nanochannel−nanopore devices for capillary evaporation study. (a) Schematic of the hybrid nanochannel−nanopore capillary evaporation measurement approach. When a water-filled hybrid nanochannel−nanopore starts drying, two menisci will form at the nanopore and the nanochannel entrances. The capillary pressure difference pins the meniscus at the nanopore entrance while pulling the other meniscus to continuously recede along the nanochannel. The evaporation flux from the nanopore can be extracted by tracking the location of the meniscus in the nanochannel. (b) Schematic diagram of the experimental setup and the hybrid nanochannel−nanopore device (cross-sectional view). The nanochannel and nanopore were fabricated in separate substrates and then bonded together. The nanopore has a conical shape (Supporting Information S2), and the narrower opening side is the vapor side. The connecting chamber cannot be seen from this cross-sectional view. (c) Microscope image of a hybrid $\frac{95\text{ nm}}{206\text{ nm}}$ nanochannel−nanopore device. There is only one hybrid nanochannel−nanopore (the middle one). The multiple nanochannels and connecting chambers are designed to facilitate the bonding alignment. (d) AFM image of the middle nanochannel in c before bonding. The nanochannel has a height of 206 nm, a width of 3.2 μm, and a roughness of 1 nm. (e) SEM image of the nanopores on the silicon nitride membrane in the same device (measured from the vapor side).

on the order of 0.1−10 fL/s based on the classical evaporation kinetics) and/or their corresponding heat transfer rates in single nanopores have made this task very challenging. In fact, none of the state-of-the-art mass or volumetric flow rate measurement techniques can directly measure such small flow rates.

We solved this challenge by using a hybrid nanochannel−nanopore based measurement approach which transforms the difficult evaporation rate measurement in a nanopore into a simple optical measurement of the receding meniscus in a rectangular 2-D nanochannel.[25] The hybrid nanochannel−nanopore based evaporation measurement requires a nanofluidic device where the to-be-tested nanopore is connected to a rectangular 2-D nanochannel with feature size (height) larger than the nanopore radius. Figure 1a shows our design of the required nanofluidic device, which consists of a thin nanopore and a long 2-D nanochannel, connected through a connecting chamber. The device is initially filled with water and placed in a vacuum chamber before the evaporation measurement. When evaporation starts, because of the difference between the nanopore radius and the nanochannel height, a capillary pressure difference would be present along the nanofluidic device, which in turn pins the meniscus at the nanopore top entrance while pulling the other meniscus to continuously recede along the nanochannel. By recording the location of meniscus in the rectangular nanochannel, the evaporation rate in the nanopore can be extracted after quantifying the contribution of water drying from the nanochannel to the meniscus receding speed.[26,27]

RESULTS AND DISCUSSION

We first used the hybrid nanochannel−nanopore devices to study evaporation from normal hydrophilic nanopores with hydrophilic inner and outer surfaces, which facilitate capillary filling of liquid water inside the nanopores and guarantee sufficient liquid supply to the liquid−vapor interface. In this work, 10 sets of the hybrid nanochannel−nanopore devices were designed and fabricated (see Figure 1b for device cross-sectional view and fabrication details in Supporting Information S1). The corresponding nanopore diameters d and nanochannel heights h are $\frac{d}{h} = \frac{27\text{ nm}}{204\text{ nm}}$, $\frac{37\text{ nm}}{200\text{ nm}}$, $\frac{57\text{ nm}}{200\text{ nm}}$, $\frac{64\text{ nm}}{200\text{ nm}}$, $\frac{71\text{ nm}}{201\text{ nm}}$, $\frac{95\text{ nm}}{206\text{ nm}}$, $\frac{102\text{ nm}}{199\text{ nm}}$, $\frac{107\text{ nm}}{199\text{ nm}}$, $\frac{146\text{ nm}}{267\text{ nm}}$, and $\frac{225\text{ nm}}{313\text{ nm}}$. In all these devices, the length of the nanopore l_p is fixed at 270 nm. The length and width of the nanochannel, l_c and w, are fixed at 230 and 3.2 μm, respectively. The connecting chamber has exactly the same height h as the nanochannel, but larger lateral dimensions of 20 × 20 μm^2. These specific dimensions of the hybrid nanochannel−nanopore devices ensure that liquid supply to the meniscus pinned at the nanopore top entrance no longer limits the mass transport and the meniscus receding in the nanochannel can be unambiguously recorded. Figure 1c shows a microscope image of the hybrid nanochannel−nanopore device ($\frac{d}{h} = \frac{95\text{ nm}}{206\text{ nm}}$). Although a device only consists of a single hybrid nanochannel−nanopore (the middle channel in Figure 1c), it actually includes an array of parallel nanochannels and connecting chambers on the glass substrate, which facilitates bonding alignment between the nanochannel and the nanopore components. The nanochannels' height is in the 200−300 nm range with a typical surface roughness less

DOI: 10.1021/acsnano.8b09258
ACS Nano 2019, 13, 3363−3372

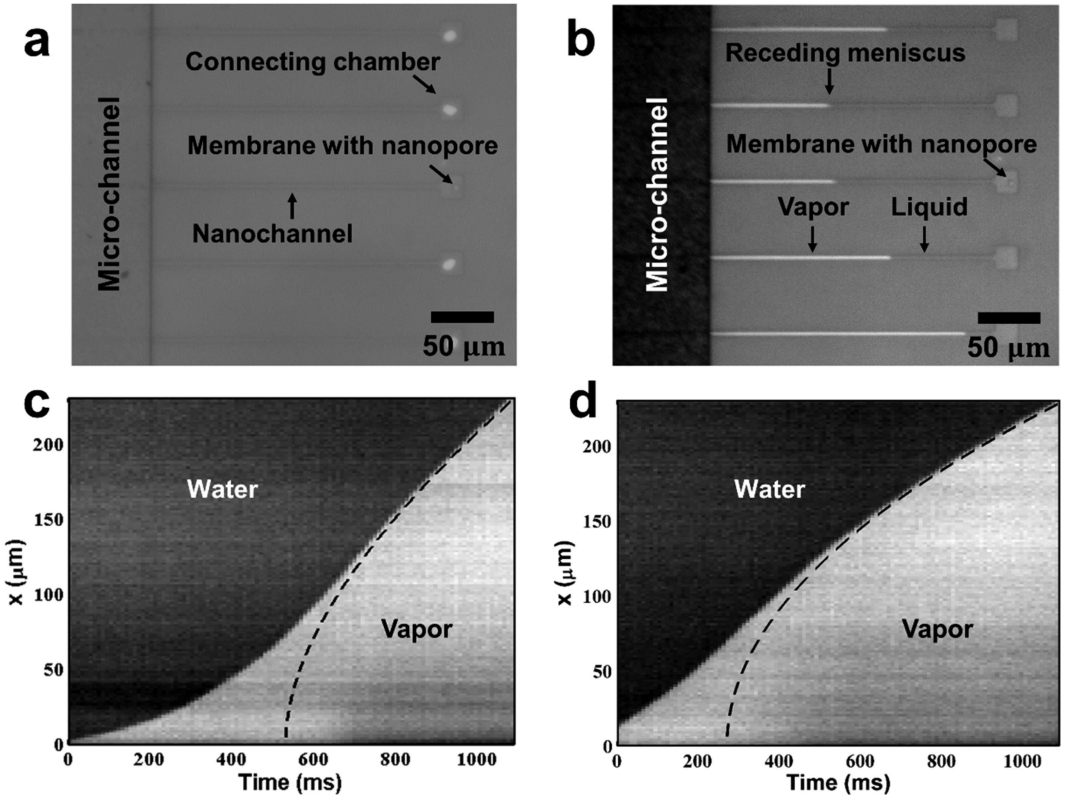

Figure 2. Measurement of kinetically limited evaporation from nanopores. (a) Snapshot of water filling in the hybrid nanochannel−nanopore device (d = 95 nm) before conducting the evaporation experiment. While the nanochannel (and the connecting chamber) that is connected with the nanopore (the middle nanochannel) was quickly filled with water, there was still trapped air in all the other nanochannels, which gradually dissolved within 10 min. (b) Snapshot of receding menisci inside the nanochannels. (c, d) Position of the receding meniscus as a function of time without PDMS blockage of the nanopore (c) and with PDMS blockage of the nanopore (d). The dashed lines in c and d plot the curve fittings based on eqs S3 and S5, respectively. Deviation of the theoretical fit from the experiments at the early stage of evaporation is due to varying vapor pressure in the microchannel.

than 5 nm, as revealed by atomic force microscopy (AFM) (see Figure 1d).

Figure 1e shows the scanning electron microscope (SEM) image of the nanopore in the suspended silicon nitride membrane. Because of the high cross-sectional area ratio between the nanochannel and the nanopore ($\frac{4wh}{\pi d^2}$), we milled multiple nanopores (2−9 in total) with the same size on the silicon nitride membrane instead of a single nanopore in order to get a sufficient meniscus receding speed in the nanochannel. The positions of the nanopores were carefully determined to minimize possible pore-to-pore interactions and boundary wall effect. For the hybrid nanochannel−nanopore devices shown in Figure 1c, three identical pores were milled onto the 4 × 4 μm^2 membrane in a triangular pattern. The suspended silicon nitride membrane is strong enough to avoid possible membrane rupture during anodic bonding as well as membrane deformation/collapse as a result of capillarity-induced negative pressure during the evaporation process (Supporting Information S3).

The evaporation measurements were performed at 22 °C in a vacuum chamber placed on an inverted microscope (Olympus IX81 ZDC) (see Figure 1b). Before the measurement, deionized water was first introduced into the device through the reservoirs and the microchannel. Although it immediately entered all the nanochannels, it would only quickly fill the entire nanochannel (and the connecting chamber) that is connected to the nanopores, because the trapped air can easily escape through the nanopores. For the closed-end nanochannels, the remaining air trapped in the nanochannels would gradually dissolve in the liquid within ~10 min.[28] A snapshot of the water filling process is shown in Figure 2a. After water had filled all nanochannels and connecting chambers, the vacuum chamber was pumped down to ~150 Pa to conduct the evaporation experiment, and the chamber pressure was actively controlled throughout the experiment to ensure water vapor could be quickly removed from the chamber and vapor transport from the interface was also not the mass transport limit. The location of the receding meniscus in the nanochannel was recorded using a high-speed camera (Hamamatsu ORCA-Flash4.0) positioned on the inverted microscope. Figure 2b shows a snapshot of the evaporation process for d = 95 nm. The evaporation process was recorded and converted to Figure 2c, which shows the position of the receding meniscus as a function of time. Since water drying through the nanochannel would also cause meniscus receding in the nanochannel,[26,27] an additional control experiment was performed after the entirety of the water evaporated. In this control experiment, after introducing water into the device, a 2 mm thick PDMS layer was placed on top of the membrane window to block evaporation through the nanopores, and the meniscus receding process in the nanochannel was recorded again (Figure 2d). The evaporation rate $\dot{Q}$ from the nanopores can be extracted by fitting these two evaporation curves with the corresponding theoretical

DOI: 10.1021/acsnano.8b09258
ACS Nano 2019, 13, 3363−3372

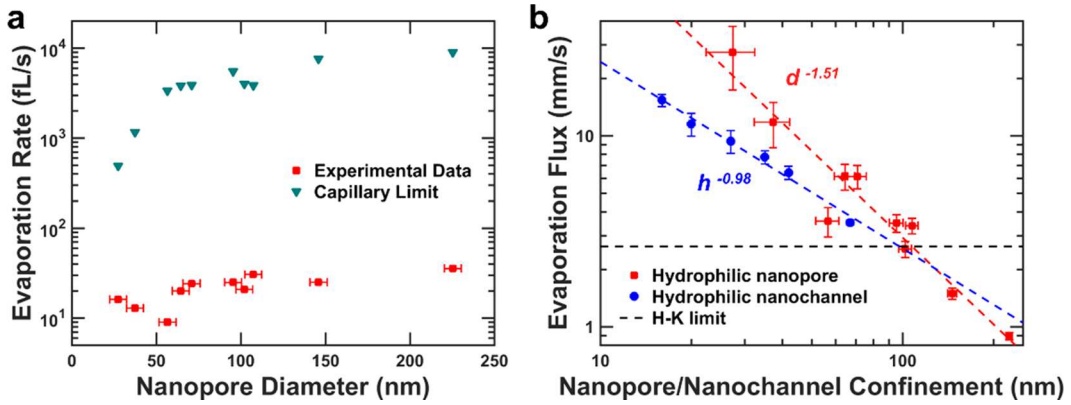

Figure 3. Experimental results of kinetically limited evaporation from normal hydrophilic nanopores with diameters ranging from 27 to 225 nm. (a) Measured evaporation rates and the corresponding theoretical predictions of the capillary limits (water supply limits). Since the capillary limits are much larger than the measured evaporation rates, evaporation in the nanopores is only limited by evaporation kinetics at the interface. (b) Measured kinetically limited evaporation fluxes in nanopores (red solid squares) and nanochannels (blue solid circles). The red and blue dashed lines are power law fits to the experimental data for the nanopores and nanochannels, respectively. The black dashed line is the theoretical prediction of the maximum evaporation flux based on the classical Hertz−Knudsen (H−K) relation. The error bars for the diameter correspond to the experimental uncertainty in the SEM characterization (Supporting Information S2). The error bars for the evaporation flux correspond to the uncertainties of pore diameter characterization and meniscus receding speed estimation. The error bars for the evaporation rates are smaller than the marker size.

models (Supporting Information S4). It is worth noting that when water starts to evaporate in the hybrid nanochannel−nanopore device, there is still water in the microchannel which would significantly influence the local vapor pressure. Therefore, we fit the meniscus receding curve only after the entirety of the water in the microchannel evaporated.

The nanopore evaporation rates for all 10 different nanopore diameters are presented in Figure 3a. We notice that the evaporation rates are different from each other and there is an increasing trend with the increasing diameter. Figure 3a also plots the liquid water transport limits due to capillary pressure difference between the menisci in the nanochannel and the nanopore (referred to as the capillary limits, see Supporting Information S5). Despite similar diameter dependence, the capillary limits are at least 1 order of magnitude larger than the corresponding measured evaporation rates, confirming that the whole evaporation process is not limited by liquid water supplies to the menisci pinned at the top entrances of the nanopores.

To further understand evaporation from the hydrophilic nanopores, we calculated the evaporation flux j for each nanopore based on the expression $j = \frac{4\dot{Q}}{\pi d^2}$ and plotted the results in Figure 3b, along with the kinetically limited evaporation fluxes from 2-D nanochannels (see our previous work in ref 25). A first key observation of Figure 3b is that the nanopore evaporation flux shows a strong dependence on the nanopore diameter. A power law fit to the evaporation flux data yields an exponent value of −1.51 with an R-squared value of 0.923. This diameter dependence of the evaporation flux in nanopore is different from that in 2-D hydrophilic nanochannels. In fact, a power law fit to the 2-D nanochannel evaporation flux data only yields an exponent value of −0.978 (R^2 = 0.984). The second key feature of Figure 3b is the ultrafast evaporation fluxes in small nanopores. When the diameter of the nanopore is below 120 nm, the measured evaporation flux exceeds the maximum theoretical limit predicted by the classical Hertz−Knudsen (H−K) relation (assuming the projected area is the same as the evaporation area and a maximum evaporation coefficient of 1, plotted with black dashed line in Figure 3b). A maximum evaporation flux of 27.4 mm/s is obtained for 27 nm nanopores at 22 °C, which is 11-fold larger than the theoretical prediction (referred to as the H−K limit later) and three times larger than the measured kinetically limited evaporation flux in 27 nm nanochannels. It is worth noting that the evaporation flux is expected to be further increase in smaller nanopores because of the strong diameter dependence. In fact, if we extend the power fitting curve to 1 nm diameter, the evaporation flux reaches ∼3 m/s at 22 °C, corresponding to a mass flux of 3×10^6 g/m^2 s. Such a high flux may corroborate the unexpected ultrahigh water permeation flux (10^6 g/m^2 s) in sub-1 nm nanoporous graphene membranes when placed between a liquid water phase and the atmosphere, which has not been well understood despite their promising potentials for water desalination.[15]

In principle, there are only two possible mechanisms that can explain the observed strong diameter dependence and the ultrafast evaporation fluxes beyond the H−K prediction in hydrophilic nanopores: (1) change in evaporation area and (2) change in evaporation coefficient. It is possible that the actual evaporation area may be significantly larger than the projected area due to surface water interactions induced meniscus extension inside nanoscale confinements[21] and/or liquid evaporating thin film outside of the nanopores.[29,30] On the other hand, the evaporation coefficient, which is believed to be bounded by unity, may exceed this value under nonequilibrium evaporation conditions and display a confinement dependence because of changes in the interfacial water structures in different confinements.[31]

By virtue of the fact that the evaporation rates from the nanopores are at least 1 order of magnitude smaller than the maximum liquid flow rates that capillary pressure can supply, the apparent contact angles at the nanopore entrances can be calculated, which are in fact quite close to 90° (Supporting Information S6). The evaporating meniscus thus would not extend much inside the nanopore and the evaporation area should not be significantly different from the projected area. As

DOI: 10.1021/acsnano.8b09258
ACS Nano 2019, 13, 3363−3372

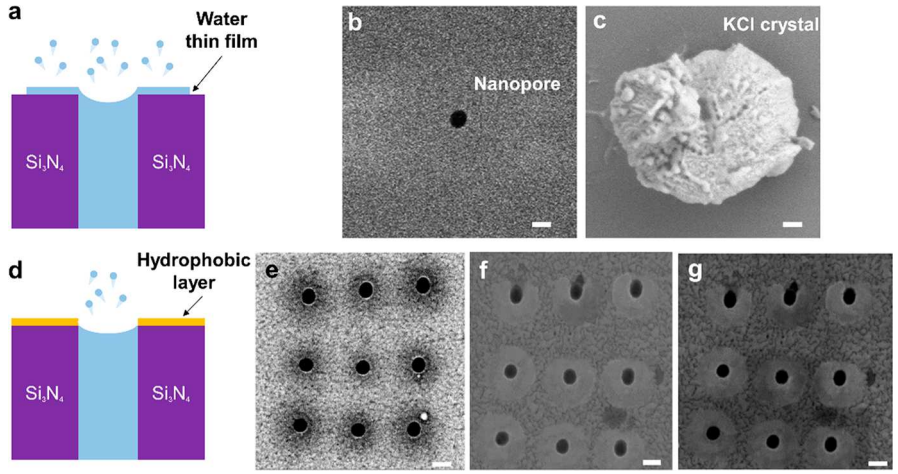

Figure 4. Proof of presence/absence of liquid water thin film outside of the nanopores. Scale bars in parts (b), (c), (e), (f), and (g) represent 200 nm. (a) Schematic of evaporation for a normal hydrophilic nanopore. Because of the strong interactions between the hydrophilic surface and liquid water, liquid water may wet certain areas outside of the nanopore after initial liquid water introduction to the nanochannel−nanopore device and form an evaporating thin film on top of the nanopore during evaporation. The actual evaporation area for the hydrophilic nanopore thus could be much larger than the nanopore cross-sectional area. (b) Top side SEM image of a nanopore (d = 146 nm) after FIB. (c) Top side SEM image of the same nanopore after the evaporation experiment using 10^{-2} M KCl solution. The presence of KCl crystals outside of the nanopore indicates that liquid water indeed can wet certain areas outside of the nanopore, which therefore may significantly contribute to evaporation. (d) Schematic of evaporation for a hydrophilic nanopore with hydrophobic top outer surface. The meniscus is pinned inside the nanopore, and consequently there is no evaporation contribution from any area outside of the nanopore. (e) Top side SEM image of nine hydrophilic nanopores with 40 nm-thick Au coating on the top of the nanopores (d = 140 nm) after FIB. (f) Top side SEM image of the same nanopores after the hydrophobic coating. The coating process does not change the diameter of the nanopores. (g) Top side SEM image of the same nanopores after the evaporation experiment using 10^{-2} M KCl solution. There are no KCl crystals outside of the nine nanopores.

a result, the change of evaporation area due to surface water interactions induced meniscus extension is unlikely to be the major mechanism for the two observed key features. It is worth mentioning that the curvature-induced change of the equilibrium vapor pressure has also been used to explain diameter-dependent evaporation of sessile droplets under saturated or near saturated vapor conditions.[32] However, this mechanism still cannot explain the observed ultrafast diameter-dependent evaporation from hydrophilic nanopores under our experimental conditions. In fact, for all the nanopores that we investigated (d = 27−225 nm), the equilibrium vapor pressure can only change by up to 1% based on the Kelvin's equation and the estimated apparent contact angle. As our experiments are always performed in a vacuum chamber (P_∞ = 150 Pa), the evaporation driving force, which is the vapor pressure difference between the interface and the ambient, will have a negligible change with the change of the nanopore diameter.

To check if there are surface water interactions induced liquid thin film outside of the nanopore (see the schematic in Figure 4a), we conducted evaporation experiments using 10^{-2} M KCl solutions instead of deionized water and examined the pore morphology before and after the experiments via SEM (see SEM images in Figure 4b,c). We noticed that there were KCl crystals outside of the nanopore after the evaporation experiment, covering circular areas with diameters of ∼2 μm. The presence of KCl crystals indicates that liquid water has at least wetted certain area outside of the nanopore and thus could form evaporating thin film, although we cannot quantitatively determine how much the wetted area would contribute to evaporation.

To further separate the evaporation contributions from outside and inside the nanopores, we created and tested hybrid nanochannel−nanopore devices which have hydrophilic nanopores with hydrophobic top outer surfaces (contact angle is 105°). These devices have similar dimensions and geometry as those prepared for studying evaporation from normal hydrophilic nanopores. They were also fabricated by almost the same fabrication process except for two additional steps: (1) we deposited a 40 nm gold thin film on the silicon nitride membrane before milling the nanopore(s), and (2) we coated a 1-octanethiol self-assembly layer on the gold thin film over the silicon nitride membrane to form the hydrophobic surface (see fabrication details in the Methods section). These two additional steps guarantee that the top outer surfaces of the resulting nanopores are hydrophobic while the inner walls are still hydrophilic. Consequently, liquid water can still fill the nanopores during water introduction, but would never wet any area outside of the nanopores and the menisci would be pinned inside the nanopores at a location very close to the top entrance (∼40 nm down from the top surface, corresponding to the thickness of the hydrophobic layer, see the schematic in Figure 4d). In this work, 8 sets of the hybrid nanochannel−nanopore devices with such hydrophobic top outer surface were fabricated and tested. The corresponding nanopore diameter d and nanochannel height h are $\frac{d}{h} = \frac{28\text{ nm}}{114\text{ nm}}$, $\frac{39\text{ nm}}{155\text{ nm}}$, $\frac{49\text{ nm}}{114\text{ nm}}$, $\frac{95\text{nm}}{114\text{ nm}}$, $\frac{110\text{ nm}}{155\text{ nm}}$, $\frac{115\text{ nm}}{155\text{ nm}}$, $\frac{233\text{ nm}}{114\text{ nm}}$, and $\frac{305\text{ nm}}{156\text{ nm}}$. The absence of liquid water outside of the nanopores (and thus the absence of evaporating thin films) was confirmed by the evaporation experiments of using 10^{-2} M KCl solution. Figure 4e−g shows the SEM images of an array of nanopores (d = 140 nm) after the FIB milling, the hydrophobic coating, and the evaporation test, respectively. No KCl crystals were detected outside of the nanopores after the evaporation test, and the nanopore size remained exactly the same compared with that before the evaporation test.

DOI: 10.1021/acsnano.8b09258
ACS Nano 2019, 13, 3363−3372

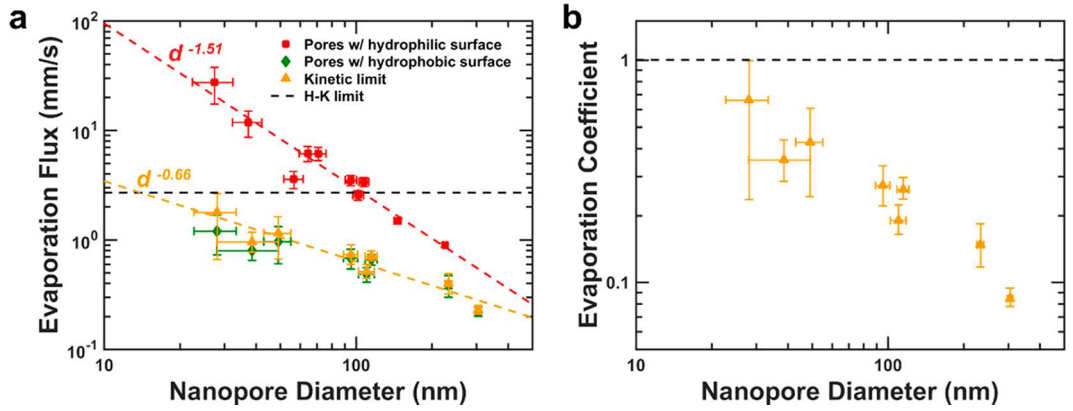

Figure 5. Experimental results of the evaporation flux and the evaporation coefficient for hydrophilic nanopores with hydrophobic top outer surface. (a) Measured evaporation fluxes of hydrophilic nanopores with hydrophobic/hydrophilic top outer surface. The red squares represent the results from hydrophilic nanopores with hydrophilic top outer surfaces, which has also been shown in Figure 3b. The green diamonds represent the results from hydrophilic nanopores with 40 nm-thick hydrophobic coating on their top outer surfaces. The orange triangles represent the "corrected" evaporation fluxes for nanopores with zero-thickness hydrophobic coating, which correspond to the true kinetic limits of the evaporation fluxes inside the nanopores. The red and orange dashed lines are power law fits to the data for the pores with hydrophilic surface and the kinetic limit, respectively. The black dashed line is the theoretical prediction of the maximum evaporation flux based on the classical Hertz-Knudsen (H−K) relation. (b) Evaporation coefficient as a function of nanopore diameter. The evaporation coefficient was extracted based on the kinetically limited evaporation flux (orange triangles in Figure 5a). The error bars on the diameter correspond to the uncertainty in the SEM characterization. The error bars for the evaporation fluxes and the effective evaporation coefficients correspond to the uncertainties of pore diameter characterization and meniscus receding speed estimation.

Figure 5a plots the measured evaporation fluxes from the eight sets of nanopores with hydrophobic top outer surface along with the results from normal hydrophilic nanopores with hydrophilic top outer surfaces. The evaporation fluxes for nanopores with hydrophobic outer surface vary from 0.22 mm/s (at d = 305 nm) to 1.2 mm/s (at d = 28 nm), corresponding to mass fluxes of 0.22×10^3−1.2×10^3 g/m^2 s and heat fluxes of 54−294 W/cm^2. Although these evaporation fluxes are still very high, there is a significant decrease when comparing them with the evaporation fluxes measured from normal hydrophilic nanopores for any given pore diameters. The evaporation fluxes for nanopores with hydrophobic outer surface are actually smaller than the H−K limit and show a different diameter dependence. To ensure that such a decrease in the evaporation flux and the different diameter dependence are not a result of additional vapor transport resistance from the thin hydrophobic layer (which is essentially a 40 nm-thick hydrophobic pore on top of the hydrophilic nanopore), we quantified the influence of the vapor transport resistance on the evaporation flux and calculated the evaporation flux for nanopores with zero-thickness hydrophobic top outer surface (Supporting Information S7). The results are also plotted in Figure 5a. These "corrected" evaporation fluxes actually correspond to the true kinetic limits of evaporation from the nanopores. We found that the "corrected" (or kinetically limited) evaporation fluxes are only slightly larger than the measured evaporation fluxes of hydrophilic nanopores with the 40 nm hydrophobic layer and they are still smaller than the H−K limit. Moreover, they are still much smaller than the evaporation fluxes measured from normal hydrophilic nanopores for any given pore diameter and show a different diameter dependence with an exponent of −0.66 (see Figure 5a).

Such a dramatic change of the evaporation flux, along with the proof of water wetting outside of the nanopore, suggests that the ultrahigh evaporation fluxes obtained from normal hydrophilic nanopores and 2-D nanochannels mainly result from extended evaporating thin films outside of the nanopores/nanochannels (see Figure 4a). Consequently, the observed diameter/height dependences for the hydrophilic nanopores/nanochannels are closely related to the area change of the extended evaporating thin films outside of the nanopores/nanochannels. The fact that the evaporation flux from the 2-D nanochannels showed almost a h^{-1} dependence ($j \propto h^{-1}$) suggests that the evaporating thin film area outside of the 2-D nanochannels must remain roughly unchanged for all nanochannels regardless of the channel height. On the other hand, the $d^{-1.5}$ dependence of the evaporation flux for normal hydrophilic nanopores ($j \propto d^{-1.5}$) indicates that the evaporating thin film area outside of the nanopores would change and continuously decrease with the decreasing nanopore diameter (otherwise a d^{-2} dependence would be observed). We found that such different changes of the evaporating thin film areas and the resulting different dependences of the evaporation fluxes on the channel/pore confinement can be qualitatively explained by different liquid water supplies to the evaporating thin films outside of the nanochannels/nanopores. Assuming that the evaporating thin films outside of different nanochannels/nanopores have the same disjoining pressure, the driving force ΔP for liquid transport from the nanochannel to the evaporating thin film would be the same for all nanochannels/nanopores regardless of their confinement. Consequently, there would be an inverse correlation between the total evaporation rate $\dot{Q}$ (which is essentially the rate of liquid water flow toward the evaporating thin film) and the total hydraulic resistance of the system ($\dot{Q} = \frac{\Delta P}{R_{hy}}$), which mainly includes the hydraulic resistance of the test nanochannels/nanopores and the hydraulic resistance of the evaporating thin film outside of the nanochannels/nanopores ($R_{hy} \approx R_n + R_{film}$). However, in the meantime, both the total evaporation rate and the hydraulic resistance of the evaporating thin film would increase with the increasing area

DOI: 10.1021/acsnano.8b09258
ACS Nano 2019, 13, 3363−3372

of the evaporating thin film. For 2-D nanochannels, since the nanochannel hydraulic resistance is relatively small, it is possible that the total hydraulic resistance would be mainly dominated by the resistance from the evaporating thin film. Therefore, the evaporation area would not change, and a constant evaporation rate should be observed, leading to the h^{-1} dependence of the nanochannel evaporation flux. In contrast, because of the drastically larger hydraulic resistance of the nanopores, the total hydraulic resistance for the nanochannel−nanopore device is dominated by the resistance from both the evaporating thin film and the nanopore itself. Decreases in the nanopore diameter and the resulting increase in the hydraulic resistance of the nanopore will inevitably decrease the total evaporation rate and the hydraulic resistance of the thin film simultaneously to ensure the product of the total hydraulic resistance and the total evaporation rate remains unchanged ($\dot{Q}(R_n + R_{film}) = \Delta P$). As a result, the nanopore evaporation flux would show a diameter dependence with an exponent value higher than −2.

Although the above hypothesis can reasonably explain the diameter dependences of the evaporation fluxes in hydrophilic nanochannels/nanopores, it cannot explain the diameter dependence of the kinetically limited evaporation fluxes, corresponding to the cases of hydrophilic nanopores with zero-thickness hydrophobic top outer surfaces where menisci are pinned at the top entrance of the nanopores and there are no evaporating thin films outside. By comparing the corresponding evaporating rates with the capillary limits, we find that almost all the pinned menisci also have apparent contact angles close to 90° (Supporting Information S6) and thus would not extend much inside the nanopores. Consequently, this diameter dependence cannot be explained by the area change of evaporating thin films of fully extended menisci, which was used to explain the diameter dependence of kinetically limited evaporation flux measured in microtubes ($j \propto d^{-1}$)[33] and to predict kinetically limited evaporation in nanopores ($j \propto d^{-0.595}$ at 90 °C).[21]

We believe that this different diameter dependence must result from the change of evaporation kinetics itself inside different nanoconfinements. The best representative of the evaporation kinetics is the evaporation coefficient, which represents the ratio of water molecules actually crossing the liquid−vapor interface to the maximum number that could cross. The evaporation coefficient is correlated with the evaporation flux by the classical H−K relation (Supporting Information S7),

$$J = \sqrt{\frac{M}{2\pi R}}\left(\sigma_e \frac{P_s(T_i^l)}{\sqrt{T_i^l}} - \sigma_c \frac{P_v}{\sqrt{T_i^v}}\right) \quad (1)$$

where σ_e and σ_c are the effective evaporation and condensation coefficients, M is the molar weight, R is the gas constant, $P_s(T_i^l)$ is the equilibrium vapor pressure at the interface, P_v is the partial pressure of the vapor in the gas phase, and T_i^l and T_i^v stand for liquid and vapor temperature at the interface, respectively.

Assuming that there is no temperature discontinuity across the liquid−vapor interface ($T_i^l = T_i^v$), the vapor pressure is the same as the ambient pressure ($P_v = P_\infty$), and the evaporation coefficient is equal to the condensation coefficient ($\sigma_e = \sigma_c$), we extracted the evaporation coefficient for each nanopore using the classical H−K relation and plotted the result in Figure 5b. The extracted evaporation coefficient decreases with the increase of the nanopore diameter, changing from 0.66 (at d = 28 nm) to 0.08 (at d = 305 nm). Such a change of the evaporation coefficient has not been reported. A recent experimental study of evaporation from alumina nanoporous membranes actually reported that the pore diameter had little effect on evaporation performance when the meniscus is pinned at the mouth of the nanopore.[34] This interesting diameter dependence cannot be explained by possible kinetics changes due to intense evaporation under nonequilibrium conditions, which has been proposed by Persad and Ward in their recent review paper.[31] In fact, Persad and Ward have proposed a model based on the quantum-mechanically based statistical rate theory (SRT) to calculate the evaporation flux and the evaporation coefficients under nonequilibrium conditions. However, based on their model, the evaporation coefficient should be larger than 1 and should not change for the same evaporation conditions,[31] which thus contradicts our observation. It is also worth noting that the extracted evaporation coefficients are consistent with limited experimental studies of nanoporous evaporators that reported the evaporation coefficients under quasi-equilibrium conditions,[35] further indicating that intense evaporation under nonequilibrium conditions may not significantly change the evaporation kinetics as proposed by the SRT model.

On the other hand, the increasing evaporation flux and evaporation coefficient with the decreasing pore diameter seem contradictory to our current understanding of interactions between water and hydrophilic surfaces. It is well-known that the strong electrostatic interactions and hydration forces between water and such surfaces would lead to the formation of a thin stagnant hydration layer (typically 2 or 3 layers of closely packed, immobile water molecules, 6−7 Å in thickness).[36−40] Since water molecules in the hydration layer are immobile, one would expect that they are harder to evaporate and thus would slow down the overall evaporation kinetics. Consequently, smaller nanopores would exhibit slower evaporation kinetics due to the increasing portion of immobile water molecules, and the opposite trend for the evaporation flux and the evaporation coefficient with respect to the pore diameter would be expected.

We hypothesize that the change of kinetically limited evaporation flux and the resulting change of the evaporation coefficient are related to the surface-charge-induced concentration change of hydronium ions (H_3O^+) inside the nanopores. It has been reported that hydronium ions in acidic aqueous solutions may perturb the local water−water structure at the liquid−vapor interface and consequently increase the possibility of water molecules leaving the liquid−vapor interface.[41] Rizzuto et al. in a recent study of Raman thermometry measurements of freely evaporating microdroplets showed that the evaporation coefficient for 0.1 M HCl solution is 45% larger than the evaporation coefficient of pure water.[41] It is well-known that silicon nitride surfaces are negatively charged when in contact with water due to dissociation of surface silanol groups.[42−46] Such negatively charged surfaces will repel co-ions and attract counterions, leading to the formation of an electrical double layer. For water confined inside the nanopores, because of the long-range electrostatic force and the resulting overlap of the electrical double layer (characterized by the Debye screening length, l_d,

DOI: 10.1021/acsnano.8b09258
ACS Nano 2019, 13, 3363−3372

which is roughly 1 μm for fresh deionized water with pH of 7 and 200 nm for CO_2 saturated water with pH of 5.68),[47] all co-ions, including OH^- and possible HCO_3^- and CO_3^{2-} due to CO_2 adsorption and dissociation will be repelled from the nanopores. In contrast, the only cations, H_3O^+ ions, will accumulate inside to neutralize the nanopore surface charges. Consequently, the co-ion concentration will be negligible and the H_3O^+ concentration will be closely related to the surface charge density σ_s and the nanopore diameter d by a simple relation $[H_3O^+] = \frac{4\sigma_s}{ed}$ (where e is electron charge) to maintain the electroneutrality.[48,49] This relation reveals that smaller nanopores would have higher concentrations of hydronium ions, which in turn could disturb the interfacial water structure outside of the hydration layer more and thus lead to higher evaporation coefficient. To verify this hypothesis, we experimentally measured ionic conductance of single silicon nitride nanopores filled with deionized water and extracted the nanopore surface charge densities and the H_3O^+ concentrations inside the nanopores based on the measured conductance (see Supporting Information S8). Our results showed that the surface charge densities of our silicon nitride nanopores are between −0.7 and −1.8 mC/m^2, which is consistent with previous studies.[42,43,45] Furthermore, our results showed that the H_3O^+ concentration inside the nanopore indeed increases with the decreasing nanopore diameter ($[H_3O^+] \propto d^{-0.75}$ according to power law fit). The different dependence of the evaporation coefficient and the H_3O^+ concentration on the pore diameter may result from change of the surface charge density due to different confinements[49] and composition of the pore walls and/or nonlinear correlation between the evaporation coefficient and the H_3O^+ concentration, which deserves further study.

CONCLUSION

In summary, we experimentally measured the kinetically limited water evaporation from individual thin silicon nitride nanopores with diameters ranging from 27 to 305 nm using a hybrid nanochannel−nanopore design. We found that the evaporation fluxes for hydrophilic nanopores with hydrophilic/hydrophobic top outer surfaces are significantly different, although both of them show strong dependence on the nanopore diameter. The evaporation fluxes for nanopores with hydrophilic outer surface show a $d^{-1.5}$ dependence and reach ultrahigh values up to 27 mm/s, being 11 times of the H−K limit. We found that such strong diameter dependence and the ultrahigh values of the evaporation flux mainly result from evaporating thin films outside of the nanopores. Consequently, such high evaporation fluxes would only be achieved in individual nanopores or small nanoporous membranes with large outer surfaces that allow the development of evaporating thin films. On the other hand, the evaporation fluxes for nanopores with zero-thickness hydrophobic top outer surface also show a strong diameter difference with an exponent of −0.66, reaching as high as 1.7 mm/s in 28 nm nanopores (which is 66% of the H−K limit). As there is no contribution from the evaporating thin film, these evaporation fluxes represent the true kinetic limits inside the silicon nitride nanopores and thus are expected to be achieved even in large nanoporous membranes without extra outer surfaces. The corresponding evaporation coefficients change from 0.66 at d = 28 nm to 0.08 at d = 305 nm. We believe that the change of the kinetically limited evaporation flux and the evaporation coefficient are closely related to surface-charge-induced concentration change of the hydronium ions inside the nanopores. Findings from this work advance our understanding of nanoscale evaporation in nature processes and enable nanopore-evaporation-based technologies for flow control in lab-on-a-chip systems, electronics cooling, and water desalination.

METHODS

Device Fabrication. The hybrid nanochannel−nanopore devices were realized using a fabrication method that includes separate fabrication of the nanopore and nanochannel components as well as a subsequent chip-to-chip aligned anodic bonding (see Figure S1). The nanopore component, including the nanopores and two liquid/vapor access reservoirs, was fabricated on a silicon substrate. As the first step, a 270 nm-thick LPCVD silicon nitride layer was deposited on a 500 μm thick, 4 in. diameter ⟨100⟩ silicon wafer (Figure S1a). Following this step, standard lithography and reactive ion etching (RIE) were used to etch square windows on one side of the wafer. The silicon wafer was then anisotropically etched along the [100] crystal direction using 30% potassium hydroxide (KOH) to create four reservoirs and a free-standing silicon nitride membrane. The etch window size and the etching time is carefully controlled to obtain desired membrane sizes for stability purposes. The reservoirs are 2 × 2 mm^2 through holes (Figure S1b). Afterward, a dual column focused ion beam (FEI Quanta 3D FEG FIB) with 10 pA current at 30 keV was used to mill the pores in the membranes (Figure S1c). The nanochannel component, including the nanochannels, connecting chambers, and microchannels that connect the nanochannels to the access reservoirs, was fabricated on a glass substrate. First, the nanochannels and the connecting chambers were created by standard lithography and RIE on a borosilicate glass wafer (Figure S1d). Next, a patterned layer of chromium was prepared using the lift-off method, serving as a mask for microchannel RIE etching (Figure S1e). The etched microchannels are 6 mm in length, 0.8 mm in width, and 3 μm in depth (Figure S1f). After the fabrication of the two separate components, both the silicon and the glass wafers were cut into 1.3 × 1.3 cm^2 chips, which were then carefully aligned with the help of a microscope and bonded together using anodic bonding at 500 V and 400 °C (Figure S1g). Before bonding, the two chips were cleaned thoroughly in Piranha solution (3:1 ratio of 98% H_2SO_4:30% H_2O_2) for 10 min.

To prepare nanopores with hydrophobic outer surface, two additional steps have been added compared to the aforementioned fabrication method. First, after fabricating a free-standing silicon nitride membrane, a 40 nm-thick gold film with 5 nm-thick titanium adhesion layer was deposited on the silicon nitride membrane using E-beam evaporator (CHA Industries). Then, nanopores were drilled through both the silicon nitride membrane and the gold layer by FIB using same method as described previously. Second, after the anodic bonding, the nanochannel−nanopore devices were immersed into a 1-octanethiol solution for 3 h to form a hydrophobic self-assembly monolayer on top of the gold layer. The 1-octanethiol solution was prepared by mixing 2 mM of 1-octanethiol (1-octanethiol ≥98.5%, Sigma-Aldrich) in ethanol (ethyl alcohol, pure ≥99.5%, Sigma-Aldrich). After the hydrophobic layer coating, the devices were rinsed with pure ethanol to remove extra thiol.

ASSOCIATED CONTENT

Supporting Information

The Supporting Information is available free of charge on the ACS Publications website at DOI: 10.1021/acsnano.8b09258.

Fabrication schematics and device images, geometry of nanopores in nanochannel−nanopore devices; elastic deformation of the membrane; theoretical models for evaporation in the hybrid nanochannel−nanopore device; water supply limit; apparent contact angle

DOI: 10.1021/acsnano.8b09258
ACS Nano 2019, 13, 3363−3372

calculation; effect of vapor transport resistance on the evaporation flux; and estimation of the hydronium ion concentration in the nanopores (PDF)

AUTHOR INFORMATION

Corresponding Author

*(C.D.) E-mail: duan@bu.edu.

ORCID

Siyang Xiao: 0000-0003-0658-0811
Ming-Chang Lu: 0000-0002-1186-0191
Chuanhua Duan: 0000-0002-5453-5321

Author Contributions

‖Y.L., H.C., and S.X. contributed equally to this work.

Notes

The authors declare no competing financial interest.

ACKNOWLEDGMENTS

This work is supported by a NSF Grant (CBET − 1805421). The authors would like to thank the Photonics Center at Boston University for the use of their fabrication and characterization facilities. The authors would also like to acknowledge Rami Yazbeck for his help in preparing nanopore devices. C.L. and M.-C.L. are thankful for the financial support from the National Chiao Tung University Short Term Research Scholarship (funded by The Ministry of Education under Taiwan's 2015 Global Networking Talent Plan), which supported C.L.'s visit to Boston University.

REFERENCES

(1) Buckley, T. N.; John, G. P.; Scoffoni, C.; Sack, L. The Sites of Evaporation within Leaves. *Plant Physiol.* **2017**, *173*, 1763−1782.

(2) Rand, R. H. Fluid-Mechanics of Green Plants. *Annu. Rev. Fluid Mech.* **1983**, *15*, 29−45.

(3) Adera, S.; Antao, D.; Raj, R.; Wang, E. N. Design of Micropillar Wicks for Thin-Film Evaporation. *Int. J. Heat Mass Transfer* **2016**, *101*, 280−294.

(4) Narayanan, S.; Fedorov, A. G.; Joshi, Y. K. Heat and Mass Transfer During Evaporation of Thin Liquid Films Confined by Nanoporous Membranes Subjected to Air Jet Impingement. *Int. J. Heat Mass Transfer* **2013**, *58*, 300−311.

(5) Xiao, R.; Maroo, S. C.; Wang, E. N. Negative Pressures in Nanoporous Membranes for Thin Film Evaporation. *Appl. Phys. Lett.* **2013**, *102*, 123103−123106.

(6) Lu, Z.; Salamon, T. R.; Narayanan, S.; Bagnall, K. R.; Hanks, D. F.; Antao, D. S.; Barabadi, B.; Sircar, J.; Simon, M. E.; Wang, E. N. Design and Modeling of Membrane-Based Evaporative Cooling Devices for Thermal Management of High Heat Fluxes. *IEEE Trans. Compon., Packag., Manuf. Technol.* **2016**, *6*, 1056−1065.

(7) Hanks, D. F.; Lu, Z.; Narayanan, S.; Bagnall, K. R.; Raj, R.; Xiao, R.; Enright, R.; Wang, E. N. Nanoporous Evaporative Device for Advanced Electronics Thermal Management. *IEEE 14th ITherm* **2014**, 290−295.

(8) Dai, X.; Famouri, M.; Abdulagatov, A. I.; Yang, R.; Lee, Y.-C.; George, S. M.; Li, C. Capillary Evaporation on Micromembrane-Enhanced Microchannel Wicks with Atomic Layer Deposited Silica. *Appl. Phys. Lett.* **2013**, *103*, 151602−151606.

(9) Dai, X.; Yang, F.; Yang, R.; Lee, Y.-C.; Li, C. Micromembrane-Enhanced Capillary Evaporation. *Int. J. Heat Mass Transfer* **2013**, *64*, 1101−1108.

(10) Ghasemi, H.; Ni, G.; Marconnet, A. M.; Loomis, J.; Yerci, S.; Miljkovic, N.; Chen, G. Solar Steam Generation by Heat Localization. *Nat. Commun.* **2014**, *5*, 4449−4456.

(11) Ni, G.; Li, G.; Boriskina, S. V.; Li, H. X.; Yang, W. L.; Zhang, T. J.; Chen, G. Steam Generation under One Sun Enabled by a Floating Structure with Thermal Concentration. *Nat. Energy* **2016**, *1*, 16126−16133.

(12) Wang, Z. H.; Liu, Y. M.; Tao, P.; Shen, Q. C.; Yi, N.; Zhang, F. Y.; Liu, Q. L.; Song, C. Y.; Zhang, D.; Shang, W.; Deng, T. Bio-Inspired Evaporation through Plasmonic Film of Nanoparticles at the Air-Water Interface. *Small* **2014**, *10*, 3234−3239.

(13) Khayet, M. Membranes and Theoretical Modeling of Membrane Distillation: A Review. *Adv. Colloid Interface Sci.* **2011**, *164*, 56−88.

(14) Alkhudhiri, A.; Darwish, N.; Hilal, N. Membrane Distillation: A Comprehensive Review. *Desalination* **2012**, *287*, 2−18.

(15) Surwade, S. P.; Smirnov, S. N.; Vlassiouk, I. V.; Unocic, R. R.; Veith, G. M.; Dai, S.; Mahurin, S. M. Water Desalination Using Nanoporous Single-Layer Graphene. *Nat. Nanotechnol.* **2015**, *10*, 459−464.

(16) Li, X. Q.; Xu, W. C.; Tang, M. Y.; Zhou, L.; Zhu, B.; Zhu, S. N.; Zhu, J. Graphene Oxide-Based Efficient and Scalable Solar Desalination under One Sun with a Confined 2d Water Path. *Proc. Natl. Acad. Sci. U. S. A.* **2016**, *113*, 13953−13958.

(17) Zhou, L.; Tan, Y. L.; Wang, J. Y.; Xu, W. C.; Yuan, Y.; Cai, W. S.; Zhu, S. N.; Zhu, J. 3d Self-Assembly of Aluminium Nanoparticles for Plasmon-Enhanced Solar Desalination. *Nat. Photonics* **2016**, *10*, 393−398.

(18) Xue, G. B.; Xu, Y.; Ding, T. P.; Li, J.; Yin, J.; Fei, W. W.; Cao, Y. Z.; Yu, J.; Yuan, L. Y.; Gong, L.; Chen, J.; Deng, S.; Zhou, J.; Guo, W. Water-Evaporation-Induced Electricity with Nanostructured Carbon Materials. *Nat. Nanotechnol.* **2017**, *12*, 317−321.

(19) Li, C. Z.; Liu, K.; Liu, H. D.; Yang, B.; Hu, X. J. Capillary Driven Electrokinetic Generator for Environmental Energy Harvesting. *Mater. Res. Bull.* **2017**, *90*, 81−86.

(20) Plawsky, J.; Fedorov, A.; Garimella, S.; Ma, H.; Maroo, S.; Chen, L.; Nam, Y. Nano-and Microstructures for Thin-Film Evaporation—a Review. *Nanoscale Microscale Thermophys. Eng.* **2014**, *18*, 251−269.

(21) Narayanan, S.; Fedorov, A. G.; Joshi, Y. K. Interfacial Transport of Evaporating Water Confined in Nanopores. *Langmuir* **2011**, *27*, 10666−10676.

(22) Lu, Z. M.; Narayanan, S.; Wang, E. N. Modeling of Evaporation from Nanopores with Nonequilibrium and Nonlocal Effects. *Langmuir* **2015**, *31*, 9817−9824.

(23) Eames, I.; Marr, N.; Sabir, H. The Evaporation Coefficient of Water: A Review. *Int. J. Heat Mass Transfer* **1997**, *40*, 2963−2973.

(24) Lu, Z.; Wilke, K. L.; Preston, D. J.; Kinefuchi, I.; Chang-Davidson, E.; Wang, E. N. An Ultrathin Nanoporous Membrane Evaporator. *Nano Lett.* **2017**, *17*, 6217−6220.

(25) Li, Y.; Alibakhshi, M. A.; Zhao, Y.; Duan, C. Exploring Ultimate Water Capillary Evaporation in Nanoscale Conduits. *Nano Lett.* **2017**, *17*, 4813−4819.

(26) Eijkel, J. C. T.; Dan, B.; Reemeijer, H. W.; Hermes, D. C.; Bomer, J. G.; van den Berg, A. Strongly Accelerated and Humidity-Independent Drying of Nanochannels Induced by Sharp Corners. *Phys. Rev. Lett.* **2005**, *95*, 256107−256110.

(27) Xie, Q.; Xiao, S.; Duan, C. Geometry-Dependent Drying in Dead-End Nanochannels. *Langmuir* **2017**, *33*, 8395−8403.

(28) Phan, V. N.; Nguyen, N.-T.; Yang, C.; Joseph, P.; Djeghlaf, L.; Bourrier, D.; Gue, A.-M. Capillary Filling in Closed End Nanochannels. *Langmuir* **2010**, *26*, 13251−13255.

(29) Mehrizi, A. A.; Wang, H. Evaporation-Induced Receding Contact Lines in Partial-Wetting Regime on a Heated Substrate. *Int. J. Heat Mass Transfer* **2018**, *124*, 279−287.

(30) Radha, B.; Esfandiar, A.; Wang, F.; Rooney, A.; Gopinadhan, K.; Keerthi, A.; Mishchenko, A.; Janardanan, A.; Blake, P.; Fumagalli, L.; et al. Molecular Transport through Capillaries Made with Atomic-Scale Precision. *Nature* **2016**, *538*, 222−225.

(31) Persad, A. H.; Ward, C. A. Expressions for the Evaporation and Condensation Coefficients in the Hertz-Knudsen Relation. *Chem. Rev.* **2016**, *116*, 7727−7767.

DOI: 10.1021/acsnano.8b09258
ACS Nano 2019, 13, 3363−3372

(32) Butt, H.-J.; Golovko, D. S.; Bonaccurso, E. On the Derivation of Young's Equation for Sessile Drops: Nonequilibrium Effects Due to Evaporation. *J. Phys. Chem. B* **2007**, *111*, 5277−5283.
(33) Buffone, C.; Sefiane, K. Investigation of Thermocapillary Convective Patterns and Their Role in the Enhancement of Evaporation from Pores. *Int. J. Multiphase Flow* **2004**, *30*, 1071−1091.
(34) Wilke, K. L.; Barabadi, B.; Lu, Z.; Zhang, T.; Wang, E. N. Parametric Study of Thin Film Evaporation from Nanoporous Membranes. *Appl. Phys. Lett.* **2017**, *111*, 171603−171607.
(35) Lee, J.; Laoui, T.; Karnik, R. Nanofluidic Transport Governed by the Liquid/Vapour Interface. *Nat. Nanotechnol.* **2014**, *9*, 317−323.
(36) Bourg, I. C.; Lee, S. S.; Fenter, P.; Tournassat, C. Stern Layer Structure and Energetics at Mica−Water Interfaces. *J. Phys. Chem. C* **2017**, *121*, 9402−9412.
(37) Alibakhshi, M. A.; Xie, Q.; Li, Y.; Duan, C. Accurate Measurement of Liquid Transport through Nanoscale Conduits. *Sci. Rep.* **2016**, *6*, 24936.
(38) Ortiz-Young, D.; Chiu, H.-C.; Kim, S.; Voïtchovsky, K.; Riedo, E. The Interplay between Apparent Viscosity and Wettability in Nanoconfined Water. *Nat. Commun.* **2013**, *4*, 2482.
(39) Wu, K.; Chen, Z.; Li, J.; Li, X.; Xu, J.; Dong, X. Wettability Effect on Nanoconfined Water Flow. *Proc. Natl. Acad. Sci. U. S. A.* **2017**, *114*, 3358.
(40) Major, R. C.; Houston, J. E.; McGrath, M. J.; Siepmann, J. I.; Zhu, X. Y. Viscous Water Meniscus under Nanoconfinement. *Phys. Rev. Lett.* **2006**, *96*, 177803.
(41) Rizzuto, A. M.; Cheng, E. S.; Lam, R. K.; Saykally, R. J. Surprising Effects of Hydrochloric Acid on the Water Evaporation Coefficient Observed by Raman Thermometry. *J. Phys. Chem. C* **2017**, *121*, 4420−4425.
(42) Smeets, R. M.; Keyser, U. F.; Krapf, D.; Wu, M.-Y.; Dekker, N. H.; Dekker, C. Salt Dependence of Ion Transport and DNA Translocation through Solid-State Nanopores. *Nano Lett.* **2006**, *6*, 89−95.
(43) Lee, C.; Joly, L.; Siria, A.; Biance, A.-L.; Fulcrand, R. m.; Bocquet, L. r. Large Apparent Electric Size of Solid-State Nanopores Due to Spatially Extended Surface Conduction. *Nano Lett.* **2012**, *12*, 4037−4044.
(44) Firnkes, M.; Pedone, D.; Knezevic, J.; Doblinger, M.; Rant, U. Electrically Facilitated Translocations of Proteins through Silicon Nitride Nanopores: Conjoint and Competitive Action of Diffusion, Electrophoresis, and Electroosmosis. *Nano Lett.* **2010**, *10*, 2162−2167.
(45) Hoogerheide, D. P.; Garaj, S.; Golovchenko, J. A. Probing Surface Charge Fluctuations with Solid-State Nanopores. *Phys. Rev. Lett.* **2009**, *102*, 256804.
(46) Waduge, P.; Hu, R.; Bandarkar, P.; Yamazaki, H.; Cressiot, B.; Zhao, Q.; Whitford, P. C.; Wanunu, M. Nanopore-Based Measurements of Protein Size, Fluctuations, and Conformational Changes. *ACS Nano* **2017**, *11*, 5706−5716.
(47) Jensen, K. L.; Kristensen, J. T.; Crumrine, A. M.; Andersen, M. B.; Bruus, H.; Pennathur, S. Hydronium-Dominated Ion Transport in Carbon-Dioxide-Saturated Electrolytes at Low Salt Concentrations in Nanochannels. *Phys. Rev. E* **2011**, *83*, 056307.
(48) Stein, D.; Kruithof, M.; Dekker, C. Surface-Charge-Governed Ion Transport in Nanofluidic Channels. *Phys. Rev. Lett.* **2004**, *93*, 035901−035903.
(49) Duan, C.; Majumdar, A. Anomalous Ion Transport in 2-Nm Hydrophilic Nanochannels. *Nat. Nanotechnol.* **2010**, *5*, 848−852.

DOI: 10.1021/acsnano.8b09258
ACS Nano 2019, 13, 3363−3372